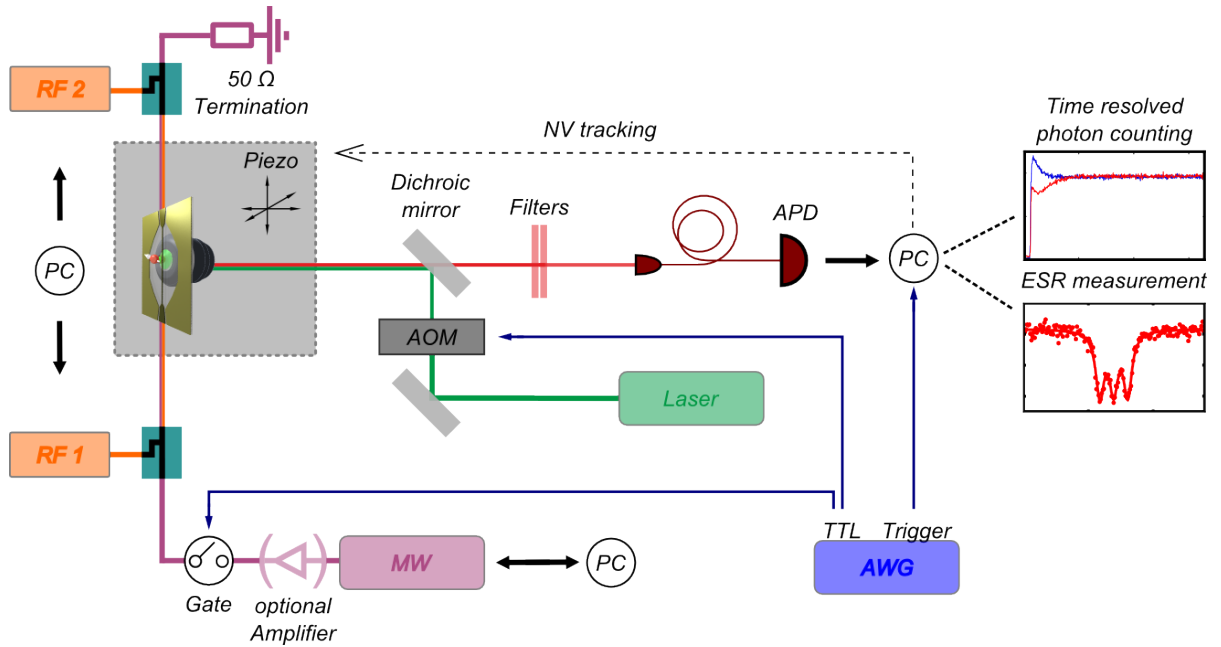


Synchronizing the dynamics of a single NV spin qubit on a parametrically coupled radio-frequency field through microwave dressing

1 Measurement setup

NV centers are inclusions in nanodiamonds spincoated on a quartz plate. We measure the fluorescence of a single NV center with the setup shown in S1. Manipulation of the NV center is performed by MW and RF fields applied through a home-made coplanar waveguide deposited on the quartz plate.



S 1: Setup. A confocal microscope is employed to read and prepare the NV electronic spin state. MW and RF currents are combined in a homemade duplexer and delivered to the NV via a coplanar waveguide lithographed on a quartz plate supporting diamond nanocrystals.

The NV fluorescence is excited non-resonantly with a 532nm laser. The photons emitted by the NV center are collected via a high numerical aperture microscope objective ($NA = 0.85$, compensated for $200 \mu\text{m}$ glass thickness) and sent through two optical filters to an avalanche photo diode (APD) (see S1). Fluorescence rates detected by the APD are in the 20 kHz range for the NV center used in this article. Measurements of Rabi oscillations were done in the saturated regime in order to be insensitive to intensity fluctuations of the laser. A 200 MHz AOM is used to form laser pulses for initialization and time-resolved readout of the NV center's spin state.

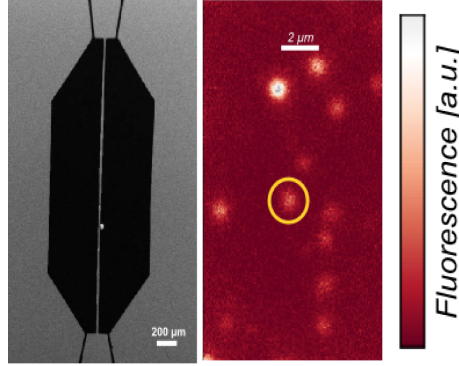
The microscope objective is mounted on a piezo-stage in order to track a single NV center. We developed a tracking program with a feedback loop which continuously maximizes the NV fluorescence. An adaptative step size routine allows for tracking a single NV over long duration while minimizing the fluorescence fluctuations due to the

tracking.

For all the experiments described in the paper we restrict ourselves to the states $|m_S = -1\rangle$ and $|m_S = 0\rangle$. A permanent magnet is used to Zeeman split the NV states $|m_S = -1\rangle$ and $|m_S = +1\rangle$ and to reach the ESLAC.

To address NV centers with MW and RF fields we patterned a home-made $50\,\Omega$ impedance coplanar waveguide on the quartz plate sample. On the central part of the waveguide an optical window is opened to allow optical access to the NV centers for fluorescence measurements. In this part the central conductor dimensions are reduced (cross section $27\,\mu\text{m} \times 0.15\,\mu\text{m}$) in order to increase locally the magnetic field (see S2).

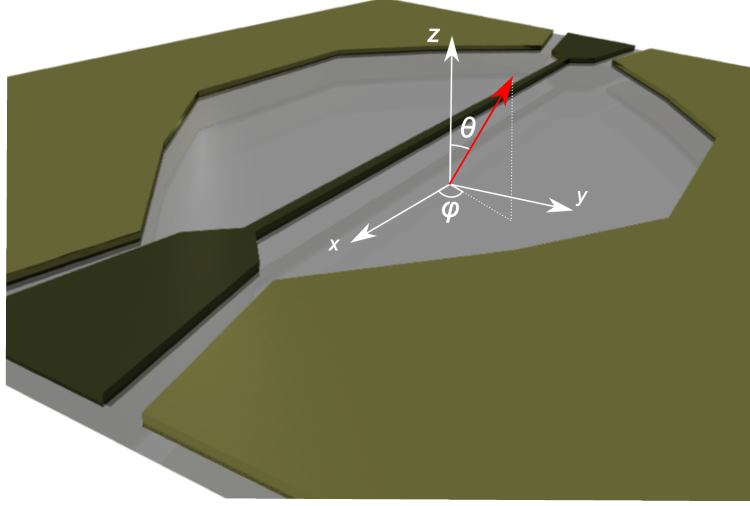
Using the Biot-Savart law we estimate the local magnetic field seen by a NV center located $5\,\mu\text{m}$ away from the waveguide (see S. 2) and with a spin orientation perpendicular to the quartz plane to be $0.235\,\text{mT/V}$, with V the applied bias voltage. The corresponding shift of the ESR resonance frequency is given by $\beta^{\text{max}} = \frac{g\mu_B}{h} \frac{B}{V} \sim 6.58\,\text{MHz/V}$.



S 2: Waveguide. Left: Electron microscope image of the waveguide used in this experiment. Right: Fluorescence scanning image of a collection of NV centers close to the waveguide. The NV center circled in yellow is the one used in this study.

2 Determination of the orientation of the NV center

Since the NV centers used in the experiment are hosted in nanodiamonds spin coated onto the sample, their alignment relative to the quartz plate is not under control. We determine the orientation of our NV center by approaching a permanent magnet with a homogeneous field gradient from two directions and detecting the corresponding Zeeman shift of the ESR peak. For the NV center presented in the main text, the polar angle (the angle between the optical axis (z) and the NV quantization axis) is estimated at $\theta \approx 68^\circ$, while the azimuthal angle (the angle between the waveguide central conductor axis (x) and the projection of the NV quantization axis onto the quartz plate, see S. 3) is estimated at $\phi \approx 71^\circ$. The imprecision inherent to the determination of the absolute magnetic field applied generates a 10% error for this estimation. The magnetic field B generated by the waveguide in the vicinity of the NV center is perpendicular to the quartz plate (Biot-Savart calculations show that the slight elevation of the waveguide and the vertical uncertainty in the nanocrystal position play negligible roles here), we have $B_{\parallel} = B \cos \theta$ and $B_{\perp} = B \sin \theta$. Hence, our NV center will experience magnetic field contributions along both directions, where components oscillating along B_{\parallel} will modulate the energy of the NV center and B_{\perp} will induce spin rotations.



S 3: NV orientation. The schematics shows the orientation of the NV quantization axis with respect to the waveguide axis ($\parallel \hat{x}$) and the optical axis ($\parallel \hat{z}$) with angles θ and ϕ .

For the experiments presented in the main text MW and RF fields are simultaneously applied through the same waveguide. As described in [1] the effects of the magnetic fields (both Rf and MW) can be categorized as follows:

- $B_{\parallel}^{\text{RF}}$: energy modulation of the two level system (TLS) at RF frequencies.
- B_{\perp}^{RF} : RF frequencies are off-resonant and hence do not induce spin transitions.
- $B_{\parallel}^{\text{MW}}$: Energy modulation at MW frequencies are too rapid compared to all other time-scales involved to be seen by the TLS.
- B_{\perp}^{MW} : Will induce spin transitions at resonance.

Note that in order for multi-photon spin transitions to occur between $|m_S = 0\rangle$ and $|m_S = -1\rangle$ (which could have been responsible for Rabi oscillations on the sidebands (Fig. 3 in the article)), an odd number of photons needs to be absorbed / emitted by the TLS in order to preserve the spin selection rules for the interaction Hamiltonian. Such effects for photon numbers larger than 1 are highly unlikely and thus neglected in our further considerations [1]. As a consequence, we can restrict our study to the Hamiltonian described in the article, where the RF and MW fields play an asymmetric role: the RF modulates the spin energy (σ_z), while the MW induces spin flips (σ_x).

3 Modeling of the NV spin dynamics in presence of RF and MW fields

For all measurements presented in the main text a static magnetic field is applied in order to Zeeman shift the levels $|m_S = -1\rangle$ and $|m_S = +1\rangle$ and restrict ourselves to the $S^{(\frac{1}{2})}$ subspace : ($|m_S = 0\rangle, |m_S = -1\rangle$), discarding the $|m_S = +1\rangle$ state. We thus model the NV center as a single two level system with spin states $|0\rangle$ and $|1\rangle$ coupled to a MW field via the σ_x -operator and to a RF field via the σ_z -operator, as justified in the previous section. The restriction to the subspace leads to a rescaling of the magnetic fields if we want to use the convenient spin 1/2 formalism in our Hamiltonian which can be rewritten: $H_{\text{int}}/g\mu_B = B_{\parallel}\sigma_z^{1/2} + B_{\perp}/\sqrt{2}\sigma_x^{1/2}$. Thus, the fields become $B_{\parallel}^{(\frac{1}{2})} = B_{\parallel}^{(1)}$ and $B_{\perp}^{(\frac{1}{2})} = \frac{1}{\sqrt{2}}B_{\perp}^{(1)}$. This is equivalent to rescaling the parametrized MW drive strength Ω_R , such that $\Omega_R = \frac{g\mu_B}{\sqrt{2}\hbar}B_{\perp}^{\text{MW}}$.

Furthermore, we make the approximation of a Markovian environment for the spin and assume that all information

of the spin's coherence passed to the environment is completely lost. This approximation although not entirely justified for NV spins in nano-diamonds allows to understand most of the experimental traces observed. However this approximation fails when trying to explain the increase of Rabi oscillation decay time as observed in Fig 4a. This effect which can be interpreted as a continuous dynamical decoupling and a protection of the spin coherence due to the continuous spin locking is beyond the scope of this article and will be investigated elsewhere.

3.1 Bloch equations

The NV spin dynamic is described by the following system of Bloch equations [2]:

$$\begin{pmatrix} \dot{u} \\ \dot{v} \\ \dot{w} \end{pmatrix} = \begin{pmatrix} -\Gamma_2^* - \Gamma_c & -(\omega - \omega_0(t)) & 0 \\ \omega - \omega_0(t) & -\Gamma_2^* - \Gamma_c & \Omega_R/2 \\ 0 & -2\Omega_R & -2\Gamma_1 - \Gamma_p \end{pmatrix} \begin{pmatrix} u \\ v \\ w \end{pmatrix} - \begin{pmatrix} 0 \\ 0 \\ \Gamma_p \end{pmatrix} \quad (1)$$

Here, u is the real part of the dipole matrix element, v the imaginary part and w is the population difference defined as $w = \sigma_{11} - \sigma_{00}$. The involved parameters are:

- Ω_R - the strength of the microwave field,
- ω - the frequency of the microwave field,
- $\omega_0(t) = \omega_0 + \delta\omega_0 \cos(\Omega_m t + \psi)$ - the resonance frequency of the TLS, which is modulated at a frequency Ω_m by an amplitude $\delta\omega_0$, at an oscillatory phase ψ (see 6).
- Γ_1 - the population decay rate from state $|m_s = -1\rangle$ to state $|m_s = 0\rangle$
- Γ_p - the relaxation due to the optical illumination, which repolarizes the spin in its ground state [2]. This process implies a transition via the metastable state. Therefore Γ_p is limited by the lifetime of the metastable state: $\Gamma_p = \Gamma_p^\infty \frac{s}{s+1}$, where $\Gamma_p^\infty \approx \frac{1}{200 \text{ ns}} = 5 \text{ MHz}$, and $s = P_{\text{opt}}/P_{\text{sat}}$ the saturation parameter of the radiative transition given by the ratio of the optical pumping power P_{opt} and the saturation power P_{sat} .
- Γ_2^* - the intrinsic spin decoherence rate.
- Γ_c - the decoherence consequent to the destruction of phase information due to optical transitions, $\Gamma_c = \Gamma_c^\infty \frac{s}{s+1}$, where $\Gamma_c \approx \frac{1}{12 \text{ ns}} = 80 \text{ MHz}$.

3.2 Bloch equations for Rabi oscillations

For Rabi oscillations only the MW and RF fields act on the spin and the laser is turned off during the spin evolution, hence $s = 0$ and the optically induced decay rates reduce to $\Gamma_p = \Gamma_c = 0$. This simplifies equation (1) to:

$$\begin{pmatrix} \dot{u} \\ \dot{v} \\ \dot{w} \end{pmatrix} = \begin{pmatrix} -\Gamma_2^* & -(\omega - \omega_0(t)) & 0 \\ \omega - \omega_0(t) & -\Gamma_2^* & \Omega_R/2 \\ 0 & -2\Omega_R & -2\Gamma_1 \end{pmatrix} \begin{pmatrix} u \\ v \\ w \end{pmatrix} \quad (2)$$

3.3 Connection between temporal decay rates and FFT linewidths

We place ourselves here in the case of resonant driving $\delta = 0$. In absence of RF field, the decay rate of Rabi oscillations ($w(t) \propto e^{-\Gamma_2^{\text{Rabi}} t} \cos(\Omega_R t)$) is given by

$$\Gamma_2^{\text{Rabi}} = \frac{\Gamma_2^*}{2} + \Gamma_1,$$

The corresponding peak in the FFT power spectrum (see Fig. 4 for an FFT amplitude spectrum) has a half width at half maximum of $\Gamma_2^{\text{Rabi}}/2\pi$. When turning on the RF field, three peaks are now visible in the FFT amplitude

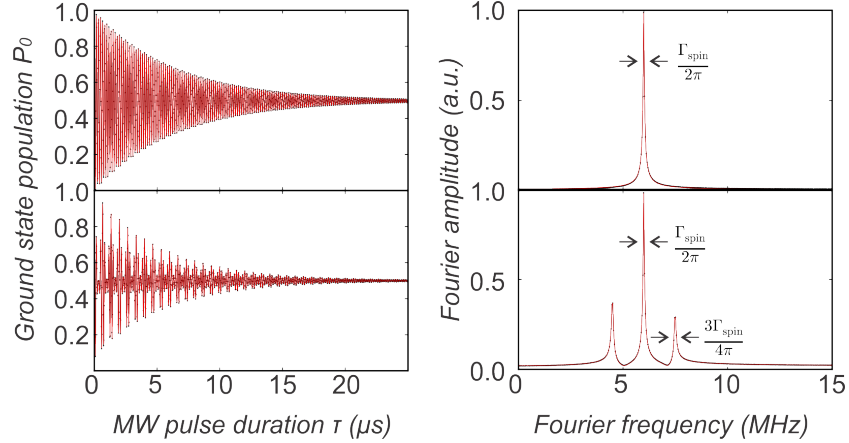
plot, splitted by $\delta\omega_0/2$. The central peak HWHM is unchanged, while the side peaks of the Mollow triplet present a 1.5 times larger damping rate (see Fig. 4). The simulated FFT amplitude spectra are fitted with the expression:

$$|A_0 + B_0 L(f, f_m, \Gamma_{\text{spin}}/2\pi) + B_+ L(f, f_m + \delta\omega_0/2, 3\Gamma_{\text{spin}}/4\pi) + B_- L(f, f_m - \delta\omega_0/2, 3\Gamma_{\text{spin}}/4\pi)|$$

where

$$L(f, f_1, \delta f) \equiv \frac{1}{f - f_1 - i\delta f}$$

is a Lorentzian whose power spectrum HWHM is δf .

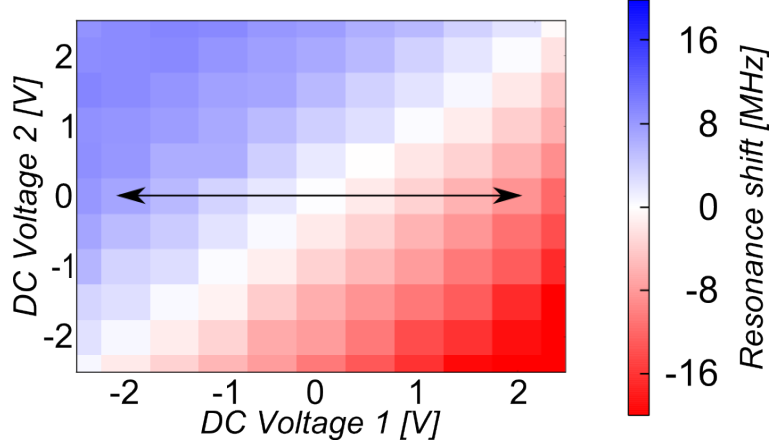


S 4: Simulated traces of Rabi oscillations and their corresponding FFT amplitude spectra, in absence and presence of a 6 MHz RF field. Black points are the results of our simulations of Bloch equations, red curve are fits (see text). The damping rate of the central peak of the triplet is the same as the one obtained in absence of RF. The side peaks of the triplet feature 1.5 times larger damping rates. In the real experiment this is not the case, due to the non-Markovian nature of the spin environment.

4 Calibration

4.1 RF-field calibration

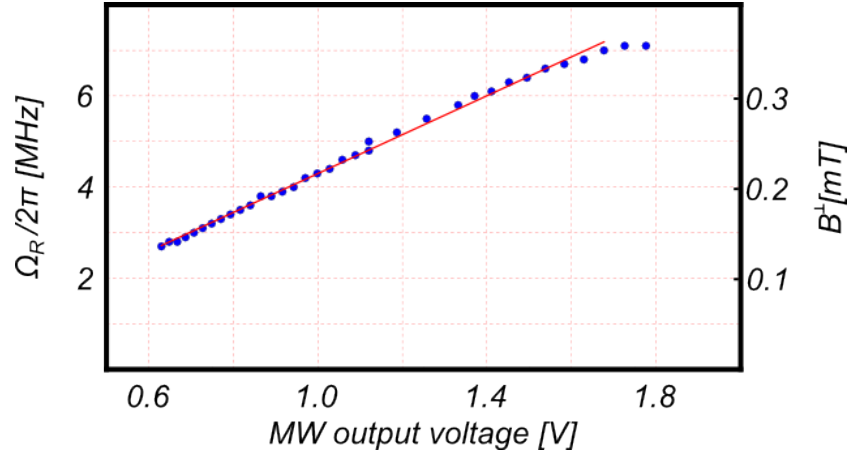
To evaluate the RF magnetic field seen by the NV center we measure how the ESR spectra are affected by the RF signals. Figure S5 shows the shifts of the ESR resonance obtained for different DC voltages applied to the waveguide input ports. The dual RF injection scheme was developed for compensating electric fields that induce quadratic shifts of the ESR frequency as a function of the applied voltage. For the NV presented in this article, increasing the DC voltage of both input channels leads to a linear shift of the ESR spectra. This firstly confirms that no residual DC field is present at the position of the NV center: indeed the shifts in the ESR spectra measured are symmetrical with respect to zero. Then, we deduce a linear dependency of the resonance shift as a function of RF amplitude voltage of $\beta = 3.6 \text{ MHz/V}$. Using the simulated value of $\beta^{\text{max}} = 6.58 \text{ MHz/V}$, we conclude that the NV center is oriented with a polar angle of $\theta = 56^\circ (\pm 3^\circ)$, which is in rough agreement with the measurements of section 2, the difference originating from the local structure of the waveguide and the impedance imperfections of the RF ports scheme.



S 5: RF calibration map. The scan along two directions allows to verify the linear shift of the spin resonance with the applied voltage. The arrow indicates the modulation axis of the experiments presented here.

4.2 MW-field calibration

To calibrate the amplitude of the microwave field seen by the NV center, we measure Rabi oscillations for varying MW input powers, see section 5.2. We verify that the measured Rabi frequency Ω_R varies linearly with the amplitude of the microwave generator output, as expected for a two level system. Using the previous expressions for Rabi frequencies (taking into account the spin 1 to spin 1/2 reduction), the corresponding magnetic field seen by the NV center falls in the range between 0.1 mT and 0.35 mT. The transmission losses in the MW port are estimated below 3 dB, rendering the use of MW power amplifiers unnecessary, which improves the long term stability of the MW scheme. This was found to be critical for accumulating Rabi traces over several days in order to obtain high quality FFT data on a single electronic spin, as presented in this paper. The NV employed in this article was chosen to present sufficient RF and MW sensitivities.

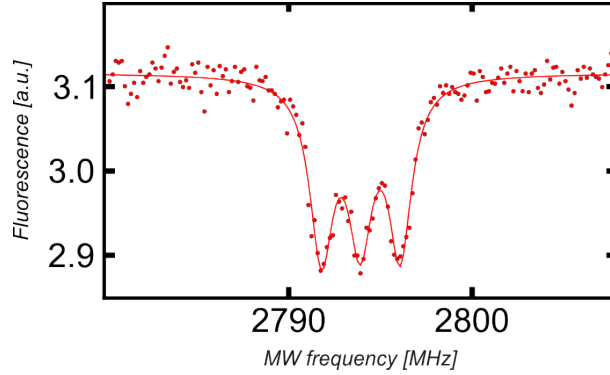


S 6: MW coupling. The MW calibration measurement (blue dots) allows to quantify Ω_R vs. injected MW power. The red line is a linear fit.

5 Measurements

5.1 ESR and hyperfine structure

Figure S7 shows the ESR spectra obtained at low microwave power (3 dBm) and in presence of a small static magnetic field of $B_{\parallel}^{\text{ext}} \approx 2.4$ mT which lifts the degeneracy between $|m_S = -1\rangle$ and $|m_S = +1\rangle$ states. The ESR peak, corresponding to the transitions between $|m_s = 0\rangle$ and $|m_s = -1\rangle$, exhibits a well resolved substructure of three peaks of width 1.4 MHz and 2.2 MHz separation. This substructure is a consequence [3] of the hyperfine interaction between the NV electronic and the ^{14}N nuclear spin of $I = 1$.

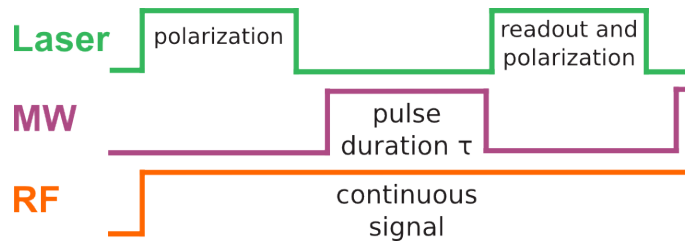


S 7: Hyperfine structure. A measurement showing the hyperfine structure in the ESR response of the NV defect under investigation.

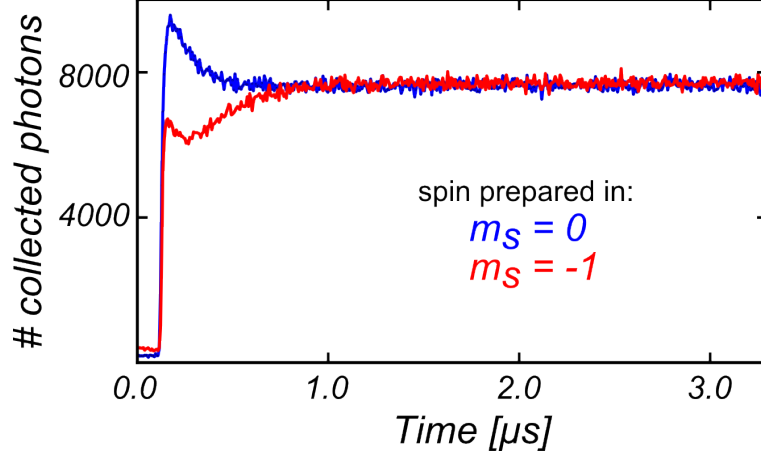
This hyperfine coupling is responsible for the subpeak structures observed in the Rabi maps in Fig. 3 and has been taken into account in the simulations (see section 6).

5.2 Rabi oscillations

We measure Rabi oscillations following the protocol depicted in figure S8: First the NV spin is initialized in its ground state $|0\rangle$ with a $5\ \mu\text{s}$ laser pulse, then the NV spin-state is manipulated with MW pulses of variable duration τ . Finally the spin state is read out by applying a laser pulse and measuring the spin-dependant fluorescence signal [4]. The emitted photons are detected by correlated photon counting measurement synchronized to the Rabi sequence, using a P7889 Multiscaler from FastComTek, see S9. Using relatively long laser pulses in our protocols allows maintaining significant amount of optical duty cycles in order to maintain a sufficiently large photon number to guarantee the reliability of the NV tracking.

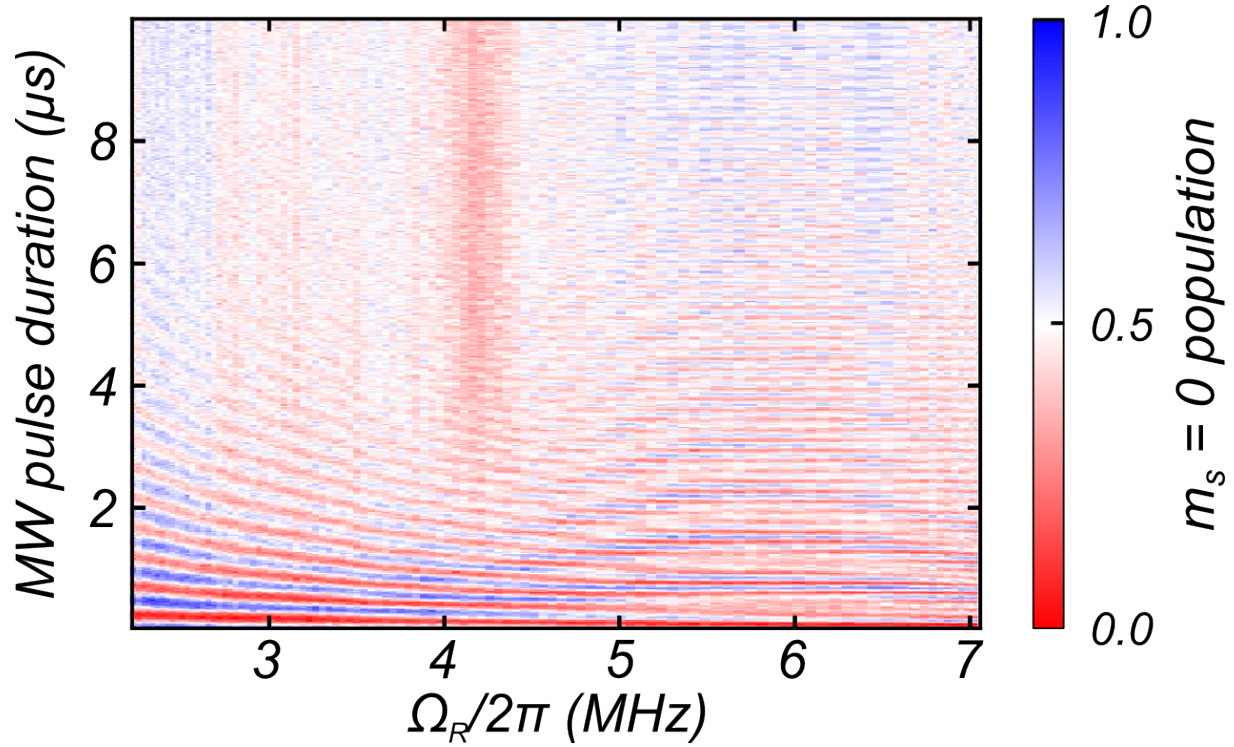


S 8: Rabi oscillation sequence. The spin is optically polarized and subsequently manipulated by the microwave field. The following laser pulse serves to readout the spin state and re-polarizes the spin prior to the next MW pulse. In our protocol, the RF field is permanently turned on.



S 9: Spin dependent fluorescence. The NV prepared in $|0\rangle$ (blue trace) emits on average more photons than the NV prepared in $|1\rangle$ (red trace).

Measurements of Rabi oscillations presented in Fig. 3 and 4 of the main text are the result of an average over 1.4×10^6 realizations and correspond to about 40 hours of continuous measurement. During this duration the position of the NV center with respect to the confocal microscope is kept constant by the home made NV-tracking program. To compensate temporal drifts of the ESR resonance due to changes in temperature or drift of the external dc magnetic field for measurements in Fig. 4, an ESR measurement is performed and the MW frequency is re-set to resonance for each new set of experimental parameters. The temporal traces used to build the FFT map of Fig. 4c are shown in S 10, clearly demonstrating the interplay of the different frequency components in terms of beating signatures as well as the enhanced coherence times T_2^{Rabi} . Notice however, that the measurement in Fig. 4b was done by continuous data acquisition over approximately 120 h, emphasizing the role of spin synchronization in compensating drifts of the MW drive strength.

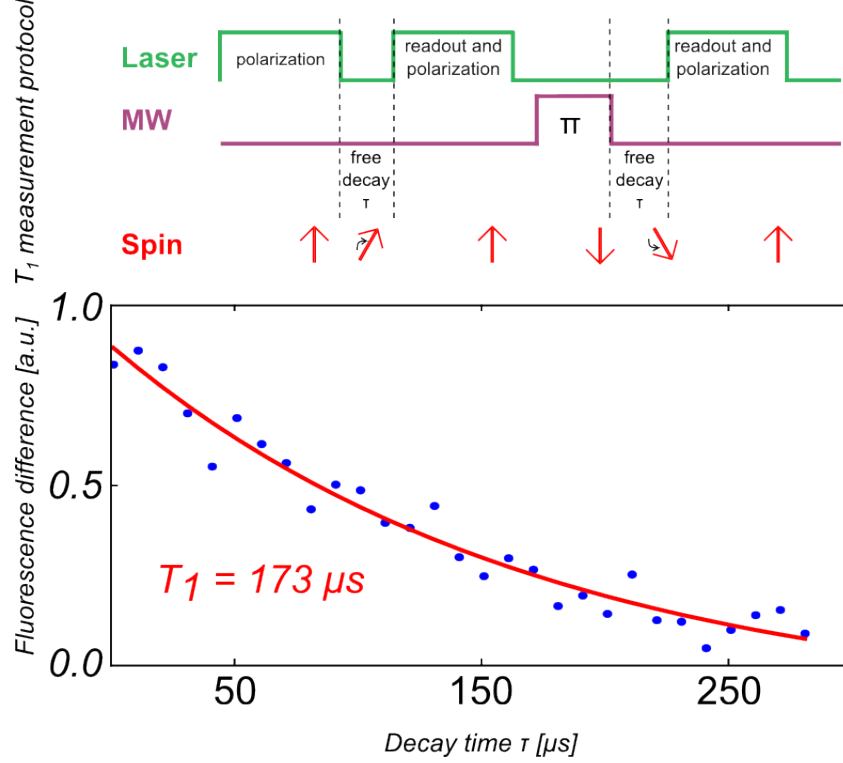


S 10: Temporal traces of Rabi oscillations for varying MW powers. The plot represents the temporal evolution of the spin population corresponding to the FFT traces of Fig. 4c, where $\Omega_m/2\pi = 6$ MHz.

To obtain sufficiently large resolution on the discrete Fourier transform spectra of Fig. 4e, 4f of the article, Rabi oscillations are measured for MW pulse duration varying between 20 ns and 5 μ s in 10 ns steps corresponding to a spectral resolution of 200 kHz. The data used for Fig. 4c correspond to [20 ns - 10 μ s] in 20 ns steps (100 kHz resolution). The high resolution data of Figure 4a and 4b correspond to the range [20 ns - 20 μ s] in 20 ns steps (50 kHz resolution).

5.3 T_1 measurements

The lifetime of the excited spin state is measured by polarizing the NV center in its excited state $|1\rangle$ or in its ground state $|0\rangle$ and measuring the population after a varying time interval τ as described in [5]. The NV is initialized in state $|0\rangle$ by optical pumping and then for every second measurement point rotated to $|1\rangle$ by a MW π -pulse (while τ stays the same), see S11. The population is then read out by optical means and fitted to an exponential decay. We find a population lifetime of $T_1 = 173 \mu$ s, as depicted in S11.



S 11: T_1 measurement. Fitting to an exponential decay yields $T_1 = 173 \mu\text{s}$. Inset: protocol and schematics of the spin evolution

5.4 T_{spin} measurements

The measured decay rate of Rabi oscillations depends on the experimental conditions, even if analytical solutions of (1) predict that in case of resonant driving ($\delta = 0$), the MW power does not contribute to the decay time of Rabi oscillations. Indeed, our measurements indicate that it slightly decreases with the MW drive strength, an effect that can not be described in our model where a Markovian bath has been employed. For example, the measurements of S6 indicates that the decay rate of Rabi oscillations follows the expression: $\Gamma_2^{\text{Rabi}} \approx 0.37 + 0.11(\Omega_R/2\pi) \text{ s}^{-1}$, Ω_R in MHz. One can see that in the spin synchronization regime which requires large Rabi frequencies, the spin linewidth, called Γ_{spin} for simplicity in the article, remains small compared to the RF frequency. For the measurements of Fig 4a,b taken in slightly different conditions due to longer time scans, the Rabi decay rate was measured at the level of $\Gamma_{\text{spin}} \approx 3 \times 10^5 \text{ s}^{-1}$. In the article we have also employed the term Γ_{spin} when describing the modulated ESR signatures and defining the resolved sideband regime. In that case, one has to take into account the additional light broadening (Γ_c) but for simplicity we have chosen to keep the same notation.

6 Simulations

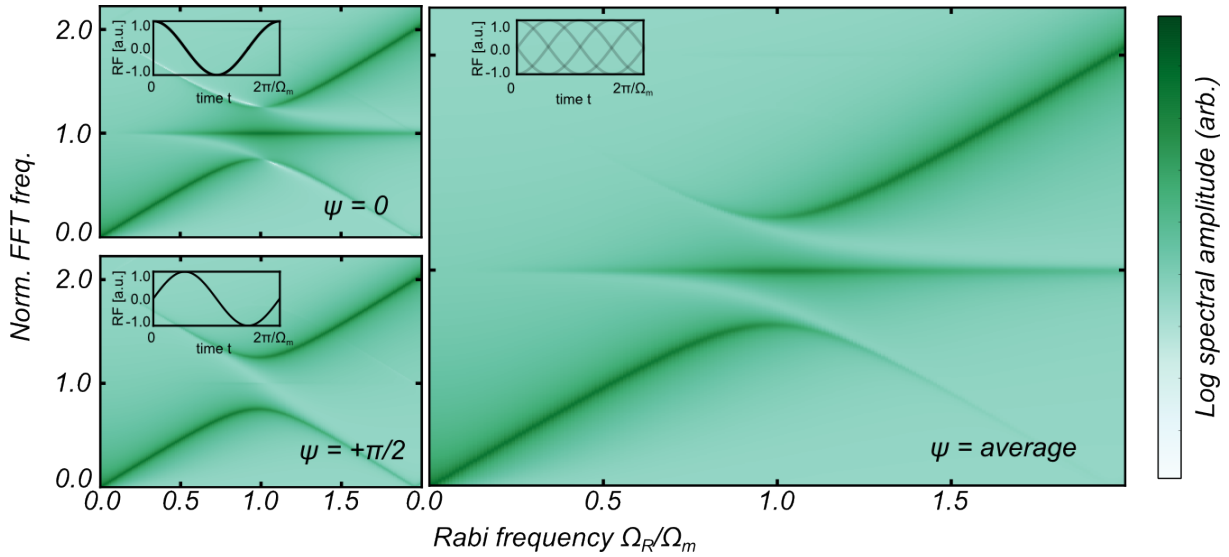
To simulate the Rabi maps presented in Fig. 3 and 4 of the main text, we solved the system of equations (2) numerically using a Runge-Kutta algorithm of 4th order developed in C. In our simulations, we use a temporal stepsize of $10^{-4} \mu\text{s}$. The initial parameters for the spin are $w(t=0) = -1$, and $u(t=0) = v(t=0) = 0$ meaning that the system is fully polarized in state $|0\rangle$ at time $t=0$. Other parameters are $\Gamma_1 = 6000 \text{ s}^{-1}$, $\Gamma_2^* = 3 \times 10^5 \text{ s}^{-1}$.

6.1 Hyperfine structure

The peaked substructure observed on the experimental maps of Fig. 3 is due to the hyperfine coupling (cf section 5.1) and was implemented in our simulations. The nuclear spin lifetime is significantly longer (~ 10 ms in [6]) than a single MW pulse duration in the sequence of the Rabi protocol, but far shorter than the whole accumulation time (hours). Thus we can consider that our measurements reflect the average over all possible nuclear spin configurations. As a consequence, the final Rabi maps of Fig. 3 were obtained by superposing three maps simulated for ω_0 , $\omega_0 - 2.1$ MHz and $\omega_0 + 2.1$ MHz.

6.2 RF phase averaging

No synchronization between the RF field and the Rabi sequence was employed in the experiments. However, in our simulations the oscillatory phase at which the laser pulse is turned off, initializing the system evolution in presence of RF and MW fields starting from the $|0\rangle$ state, do play a role as in classical phase lock loops. The derived FFT spectra thus strongly depend on the oscillatory phase, ψ , as can be seen in figure S12. When the NV is driven at $\Omega_R = \Omega_m$, the frequency component at Ω_m is only present in the FFT for $\psi = 0[\pi]$, where simultaneously, the components at $\Omega_m \pm \delta\omega_0/2$ vanishes. Here, the phase difference ψ is defined such that for $\psi = 0$ at $t = 0$ the spin is polarized in state $|0\rangle$ and the oscillator is at maximum amplitude, corresponding to $\omega_0(t = 0) = \omega_0 + \delta\omega_0$. In the simulated maps of Fig. 4 we averaged the temporal Rabi traces over ψ before calculating the FFT map. This explains why all components are visible in the spectra.



S 12: Influence of the RF oscillatory phase on the Rabi maps. The FFT maps on the left are taken at different initial oscillation states: the left upper trace are obtained when the RF field is maximum at $t = 0$ ($\psi = 0$), the lower ones when it is at zero ($\psi = \pi/2$). The right map is obtained by averaging over the oscillatory phase in order to describe the experimental situation.

7 Doubly dressed spin

In order to understand the features of Fig. 3 and Fig. 4 of the article, we present an interpretation in term of double dressing of our system with a MW and a RF field. We find that by probing the MW dressed spin with the RF field we can explain the triple peak features and the "anti-crossing" in the FFT spectra. Reversely, this picture also leads to an explanation of the Bessel-like dependence of the effective Rabi frequency. We consider the total

Hamiltonian:

$$H_{\text{tot}} = H_0 + H_{\text{MW}} + H_{\text{int}} \quad (3)$$

with

$$\begin{aligned} H_0 &= \hbar\omega_0\hat{\sigma}_z + \hbar\Omega_{\text{m}}\hat{a}^\dagger\hat{a} + \hbar\omega\hat{b}^\dagger\hat{b} \\ H_{\text{MW}} &= \hbar\Omega_R^v(\hat{b}^\dagger + \hat{b})\sigma_x \\ H_{\text{int}} &= \hbar\kappa^v(\hat{a}^\dagger + \hat{a})\sigma_z \end{aligned}$$

The generic eigenstates of H_0 are $|m_s, N, M\rangle$, where $m_s = 0, 1$ is the spin state, N the photon number and M the phonon number. Their eigenenergies are:

$$E_{|m_s, N, M\rangle}/\hbar = m_s\omega_0 + N\omega + M\Omega_{\text{m}}.$$

7.1 Dressing the spin with the MW field

We first dress the system with the microwave field and apply H_{MW} . It does not modify the phonon number, so we can use the usual dressed atom equations: we introduce the multiplicities

$$\mathcal{E}_N = \{|1, N-1\rangle, |0, N\rangle\},$$

where N is the number of total excitations. If $\delta \equiv \omega - \omega_0$, we have an interaction Hamiltonian in the subspace:

$$H_{\text{int}}^{\text{MW}} = \begin{pmatrix} 0 & \frac{\Omega_R^v\sqrt{N}}{2} \\ \frac{\Omega_R^v\sqrt{N}}{2} & \delta \end{pmatrix},$$

where the factor of $\frac{1}{2}$ arises from the rotating wave approximation. The new eigenstates are now $|\pm_N\rangle$ with energies (setting the energy of the ground state $|0, 0\rangle$ to $\hbar\omega/2$):

$$E_{|\pm_N\rangle}/\hbar = N\omega - \frac{\delta}{2} \pm \frac{1}{2}\sqrt{\delta^2 + N\Omega_R^v{}^2}$$

featuring a splitting of

$$\Delta(N) \equiv \sqrt{\delta^2 + N\Omega_R^v{}^2}.$$

If we define the angle Θ_N in $[0, \pi]$ by :

$$\tan \Theta_N = -\Omega_R^v\sqrt{N}/\delta,$$

then the eigenstates can be written as:

$$\begin{aligned} |+_N\rangle &= \cos \frac{\Theta_N}{2} |1, N-1\rangle + \sin \frac{\Theta_N}{2} |0, N\rangle \\ |-_N\rangle &= -\sin \frac{\Theta_N}{2} |1, N-1\rangle + \cos \frac{\Theta_N}{2} |0, N\rangle. \end{aligned}$$

The σ_z operator has no effect between multiplicities having a different N and is described in the basis $\{|-_N\rangle, |+_N\rangle\}$ by:

$$\sigma_z|_{\mathcal{E}_N} = \begin{pmatrix} \sin^2 \frac{\Theta_N}{2} & -\cos \frac{\Theta_N}{2} \sin \frac{\Theta_N}{2} \\ -\cos \frac{\Theta_N}{2} \sin \frac{\Theta_N}{2} & \cos^2 \frac{\Theta_N}{2} \end{pmatrix}.$$

Importantly, this point shows that the σ_z operator now has some non-trivial action on the new dressed eigenstates. Thus, the RF field described by H_{int} can induce rotations of the dressed spin.

7.2 Dressing the MW-dressed spin state with the RF field

As mentioned in the main text, in the picture of dressed states the role of longitudinal and transversal magnetic field components are interchanged, as the dressed spin is polarized along an axis in the equatorial plane of the Bloch sphere. Hence, a magnetic field along the z direction oscillating at frequency Ω_m can induce transitions between the dressed states if the field is resonant with the energy splitting, Ω_R .

We add the phonon field and the generic eigenstates are now of the form: $|\pm_N\rangle \otimes |M\rangle \equiv |\pm_N, M\rangle$. The interaction Hamiltonian couples the eigenstates that present a phonon number difference of ± 1 and we can thus restrict our considerations to the multiplicity:

$$\tilde{\mathcal{E}}_{N,M} = \{|+N, M-1\rangle, |-N, M\rangle\}.$$

The uncoupled energies are:

$$E_{|\pm_N, M\rangle}/\hbar = N\omega - \frac{\delta}{2} \pm \frac{\Delta(N)}{2} + M\Omega_m$$

and using $\sin \Theta_N = -\Omega_R^v \sqrt{N}/\sqrt{\delta^2 + N\Omega_R^{v2}}$, the interaction Hamiltonian can be written in the multiplicity $\tilde{\mathcal{E}}_{N,M}$ as:

$$\begin{pmatrix} 0 & \kappa_{N,M}/2 \\ \kappa_{N,M}/2 & \Omega_m - \Delta(N) \end{pmatrix} \quad (4)$$

with

$$\kappa_{N,M} \equiv -\frac{\kappa^v \sqrt{M}}{2} \sin \Theta_N = \frac{\kappa^v \sqrt{M}}{2} \frac{\Omega_R^v \sqrt{N}}{\sqrt{\delta^2 + N\Omega_R^{v2}}}.$$

The new eigenstates $|\pm_{N,M}\rangle$ have energies

$$E_{|\pm_{N,M}\rangle}/\hbar = N\omega - \frac{\delta}{2} + \frac{\Delta(N)}{2} + (M - \frac{1}{2})\Omega_m \pm \frac{1}{2}\Delta(N, M), \quad (5)$$

where

$$\Delta(N, M) \equiv \sqrt{(\Omega_m - \Delta(N))^2 + \kappa_{N,M}^2}$$

and

$$\begin{aligned} |+_{N,M}\rangle &= \cos \frac{\Theta_M}{2} |+N, M-1\rangle + \sin \frac{\Theta_M}{2} |-N, M\rangle \\ |-_{N,M}\rangle &= -\sin \frac{\Theta_M}{2} |+N, M-1\rangle + \cos \frac{\Theta_M}{2} |-N, M\rangle \end{aligned}$$

and

$$\tan \Theta_M = -\kappa_{N,M}/(\Omega_m - \Delta(N)).$$

For a classical description of the MW and RF field, $\sqrt{N}\Omega_R^v \rightarrow \Omega_R$, $\sqrt{M}\kappa_{N,M}^v \rightarrow \delta\omega_0$, the splitting becomes $\Delta(N, M) \rightarrow \Delta_{\text{Mollow}}$, with

$$\Delta_{\text{Mollow}} = \sqrt{\left(\Omega_m - \sqrt{\delta^2 + \Omega_R^2}\right)^2 + \left(\frac{\delta\omega_0}{2}\right)^2 \frac{\Omega_R^2}{\delta^2 + \Omega_R^2}}.$$

In case of resonant pumping $\delta = 0$, it simplifies to:

$$\Delta_{\text{Mollow}} = \sqrt{(\Omega_m - \Omega_R)^2 + \left(\frac{\delta\omega_0}{2}\right)^2}. \quad (6)$$

The frequencies that are present in the Rabi oscillations have to be found in the spectrum of allowed transitions of the σ_z operator between the eigenstates of the doubly dressed spin. The FFT spectra of the temporal Rabi traces can be interpreted as a result of a "fluorescence cascade" of the doubly dressed spin. The observed frequency components are thus transitions allowed by the selection rules of the σ_z -operator, see S 13:

$|+_{N,M+1}\rangle \leftrightarrow |-_{N,M}\rangle$ oscillating at $\Omega_m + \Delta(N, M)$

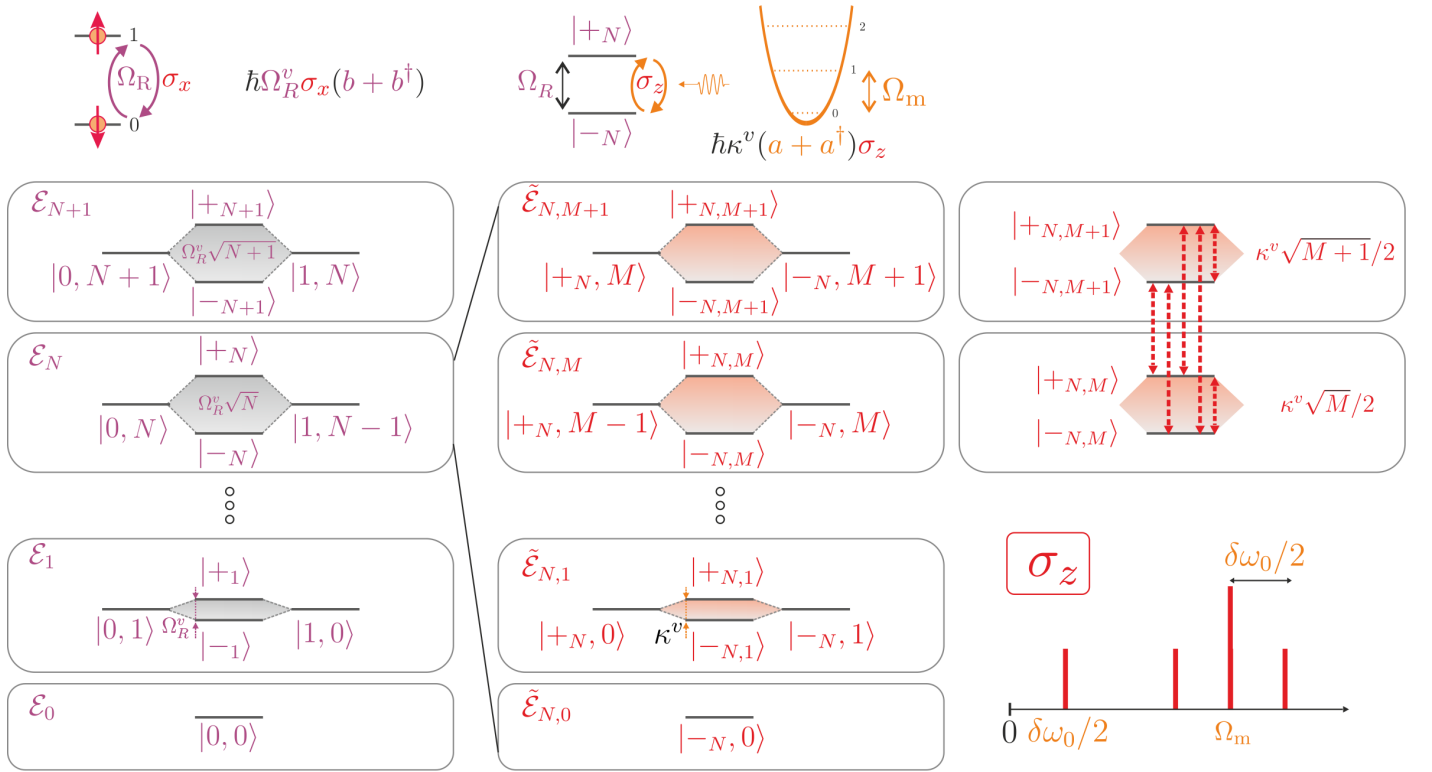
$|-_{N,M+1}\rangle \leftrightarrow |-_{N,M}\rangle$ oscillating at Ω_m

$|+_{N,M+1}\rangle \leftrightarrow |+_{N,M}\rangle$ oscillating at Ω_m

$|-_{N,M+1}\rangle \leftrightarrow |+_{N,M}\rangle$ oscillating at $\Omega_m - \Delta(N, M)$

$|+_{N,M}\rangle \leftrightarrow |-_{N,M}\rangle$ oscillating at $\Delta(N, M)$

The last term is not visible in case of perfect resonant pumping ($\delta = 0$). Due to state preparation in the ground state of the spin, our system is displaced from equilibrium at $t = 0$. Thus the analysis of its relaxation towards equilibrium following this initial displacement, which is a sort of percussional response, reveals all the allowed transitions previously calculated. Their relative weight can be computed following the previous reasoning.



S 13: Left: the spin is first dressed by the MW field. Center: the oscillator/RF field acting in the dressed base. Right: the transitions contributing to the measured Rabi oscillations close to the mechanical frequency.

7.3 Bloch - Siegert shift

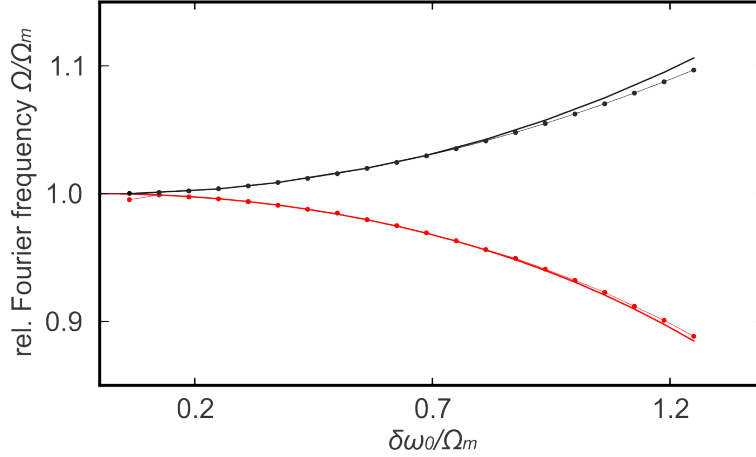
When restricting the considered transitions to the ones within multiplicities $\tilde{\mathcal{E}}_{N,M}$ we have implicitly made a rotating wave approximation (RWA) for the RF field, as reflected by the factors of $1/2$ in the off-diagonal elements of Hamiltonian (4). Here, the assumption that $\delta\omega_0 \ll \Omega_m$ is not necessarily valid and for large values of $\delta\omega_0$ we have to consider effects like the Bloch - Siegert shift for the phonon field, which is indeed visible in our simulations and experimental data, as mentioned in the main text. According to [7] the minimum splitting between the perturbed energy eigenstates occurs at $\Omega_R = \Omega_R^\odot$, with

$$\Omega_R^\odot \equiv \Omega_m - \frac{\left(\frac{\delta\omega_0}{4}\right)^2}{\Omega_m} - \frac{5\left(\frac{\delta\omega_0}{4}\right)^4}{4\Omega_m^3} + \frac{61\left(\frac{\delta\omega_0}{4}\right)^6}{32\Omega_m^5}. \quad (7)$$

We define Ω_R^* as the MW power for which the FFT component of the σ_z operator oscillating at the mechanical frequency is maximum. Its expression is given by inverting the previous equation [7]:

$$\Omega_R^* \equiv \Omega_R + \frac{\left(\frac{\delta\omega_0}{4}\right)^2}{\Omega_R} + \frac{\left(\frac{\delta\omega_0}{4}\right)^4}{4\Omega_R^3} - \frac{36\left(\frac{\delta\omega_0}{4}\right)^6}{32\Omega_R^5}. \quad (8)$$

These expressions are in quantitative agreement with simulations and in qualitative agreement with experimental data, see S 14.



S 14: Effect of the Bloch - Siegert shift. The MW power required for reaching the minimum splitting (Ω_R^\odot , red) and the maximum spectral density (Ω_R^* , black) at Ω_m depends on the RF drive amplitude. The dots are data points obtained from numerical simulations and fat solid lines are the analytical expressions given above.

References

- [1] Lilian Childress and Jean McIntyre. Multifrequency spin resonance in diamond. *Physical Review A*, 82(3), September 2010.
- [2] A. Dréau, M. Lesik, L. Rondin, P. Spinicelli, O. Arcizet, J.-F. Roch, and V. Jacques. Avoiding power broadening in optically detected magnetic resonance of single NV defects for enhanced dc magnetic field sensitivity. *Physical Review B*, 84(19):1–8, November 2011.
- [3] S. Felton, A. Edmonds, M. Newton, P. Martineau, D. Fisher, D. Twitchen, and J. Baker. Hyperfine interaction in the ground state of the negatively charged nitrogen vacancy center in diamond. *Physical Review B*, 79(7):1–8, February 2009.
- [4] F. Jelezko, T. Gaebel, I. Popa, A. Gruber, and J. Wrachtrup. Observation of Coherent Oscillations in a Single Electron Spin. *Physical Review Letters*, 92(7):1–4, February 2004.
- [5] A. Jarmola, V. Acosta, K. Jensen, S. Chemerisov, and D. Budker. Temperature- and Magnetic-Field-Dependent Longitudinal Spin Relaxation in Nitrogen-Vacancy Ensembles in Diamond. *Physical Review Letters*, 108(19):1–5, May 2012.

- [6] M V Gurudev Dutt, L Childress, L Jiang, E Togan, J Maze, F Jelezko, A S Zibrov, P R Hemmer, and M D Lukin. Quantum register based on individual electronic and nuclear spin qubits in diamond. *Science (New York, N.Y.)*, 316(5829):1312–6, June 2007.
- [7] C Cohen-Tannoudji, J Dupont-Roc, and C Fabre. Quantum calculation of the higher order terms in the Bloch-Siegert shift. *J. Phys. B: Atom. Molec. Phys.*, 6(August):214–217, 1973.